An Asynchronous Sampling-Based 128×128 Direct Photon-Counting X-Ray Image Detector with Multi-Energy Discrimination and High Spatial Resolution

Hyun-Sik Kim, *Student Member, IEEE*, Sang-Wook Han, Jun-Hyeok Yang, Sunil Kim, Young Kim, Sangwook Kim, Dae-Kun Yoon, Jun-Su Lee, Jae-Chul Park, Younghun Sung, Seong-Deok Lee, Seung-Tak Ryu, *Member, IEEE*, and Gyu-Hyeong Cho, *Senior Member, IEEE*

***Abstract*—This paper presents a direct photon-counting X-ray image detector with a HgI_2 photoconductor for high-quality medical imaging applications. The proposed sampling-based charge preamplifier with asynchronous self-reset enables a pixel to detect single X-ray photon energy with higher sensitivity and faster processing rate. The use of the correlated double sampling enabled by the sampling-based architecture also reduces flicker noise and contributes to the achievement of high pixel-to-pixel uniformity. Discrimination of the energy level of the detected X-rays is performed by the proposed compact in-pixel ADC with low power consumption. Three 15-bit counters in each pixel count up energy-discriminated photons for the reconstruction of multi-spectral X-ray images. A 128×128 X-ray image detector with a pixel size of $60 \times 60\ \mu m^2$ is implemented and measured using a 0.13-μm/0.35-μm standard CMOS process. It discriminates 3 energy levels of photon energy with a gain of 107 mV/ke^- and a static power consumption of 4.6 μW/pixel. The measured equivalent noise charge (ENC) and minimum detectable energy level of the detector pixel are 68 e^- rms and 290 e^-, respectively. The measured maximum threshold dispersion in the pixel array is 164 e^- rms without any calibration. The functionality of our chip is also successfully demonstrated using real X-ray images.**

***Index Terms*—ADC, arrays, CMOS, detectors, image sensors, photoconductor, photon counting, photonics, preamplifiers, sampling-based circuits, switches, x-ray imaging.**

I. Introduction

EXISTING and emerging applications of digital X-ray imaging can be found in a variety of fields including medical imaging, crystallography, security, astrophysics, and particle physics research. The basic principle of digital X-ray imaging is illustrated in Fig. 1. A digital X-ray image detector detects X-ray photons that are transmitted from X-radiation sources and passed through a target object. The sensing element absorbs X-ray photons in a target range of energies and produces a charge packet proportional to the energy of the absorbed X-ray photon. The electronic circuit takes the charge packet generated by the sensing element and produces a voltage signal that is proportional to the detected amount of charge. The voltage signal is then converted into a digital signal by A/D conversion. Finally, the resulting digital data are transferred to the external host system for the reconstruction of X-ray images.

In Fig. 1, the sensing elements can be classified according to their principle of operation: direct conversion type and indirect conversion type. In the direct conversion type, the semiconductor photoconductor converts X-ray photons into charge packets by the photo-electric effect, and the generated charge packet is directly processed by an interconnected CMOS front-end ASIC. In the indirect conversion type, X-ray photons are absorbed in the scintillator material, and then a secondary visible light flash is produced from the scintillator as a result of an ionizing particle interacting with the scintillator. A CMOS front-end ASIC under the scintillator detects a visible light flash by using a silicon photodiode. Compared with the indirect type, the direct conversion method has higher X-ray-to-charge conversion efficiency and position resolution. Therefore, direct-type sensing is suitable for medical imaging applications, where dose efficiency and image quality are especially important.

When hit by an X-ray photon, the photoconductor generates a charge packet that drifts toward the electrode. In the conventional detectors [1], [2], the charge generated by a large number of detected photons is integrated in a continuous-time fashion during the exposure time so as to produce an X-photon transmission intensity image. However, by doing so, the photon energies can be added together without distinction of individual X-ray photons. Furthermore, noise is added to the useful signal during the charge integration time. To solve these problems, the photon counting method was suggested in [3]. The method effectively rejects noise, and the individual X-ray photon energy can be measured. Moreover, it allows immediate discrimination of X-ray photons with different energy levels, as shown in Fig. 2. Note that several different X-ray images can be achieved

Manuscript received May 15, 2012; revised August 23, 2012; accepted September 12, 2012. Date of publication December 03, 2012; date of current version January 24, 2013.This paper was approved by Associate Editor Boris Murmann.

H.-S. Kim, J.-H. Yang, S.-T. Ryu, and G.-H. Cho are with the Department of Electrical Engineering, KAIST, Daejeon 305-701, Korea (e-mail: rutan@kaist.ac.kr).

S.-W. Han, S. Kim, Y. Kim, S. Kim, D.-K. Yoon, J.-S. Lee, J.-C. Park, Y. Sung, and S.-D. Lee are with the Samsung Advanced Institute of Technology, Samsung Electronics Co. Ltd., Yongin 446-712, Gyeonggi-do, Korea.

Color versions of one or more of the figures in this paper are available online at http://ieeexplore.ieee.org.

Digital Object Identifier 10.1109/JSSC.2012.2221196

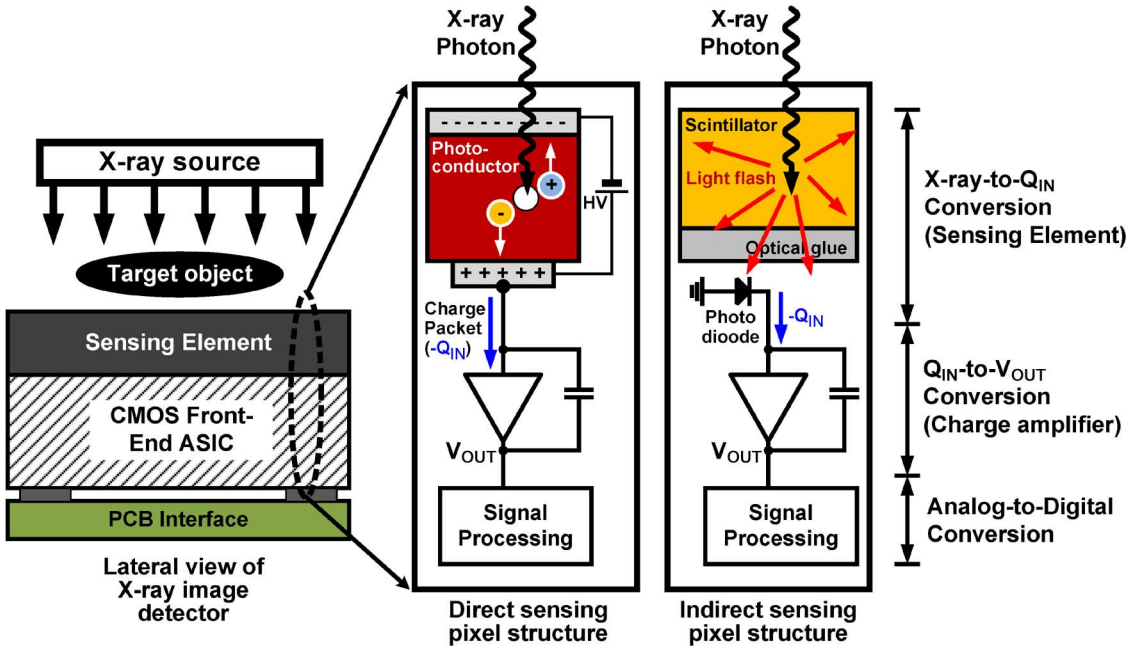

Fig. 1. Principle and structure of X-ray image detector system.

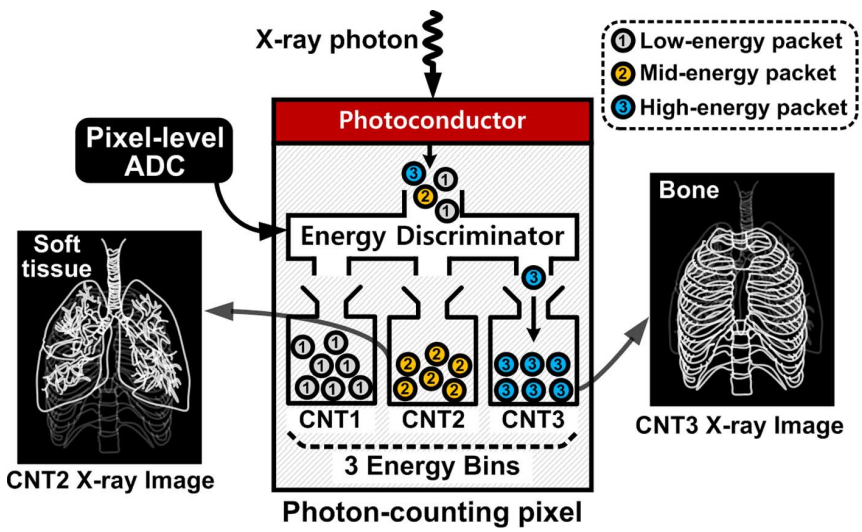

Fig. 2. Basic concept of the multi-energy photon counting.

depending on the different energy levels of the absorbed X-rays [4]. For example, in medical radiography, the photon counting with multi-energy discrimination enables separation of soft tissues from bones, providing a compositional analysis through multispectral X-ray imaging.

The X-ray image detector consists of one- or two-dimensional arrays of photon detecting pixels. Fig. 3 shows a conventional direct photon-detecting (photon-counting) pixel topology and illustrates the photon-counting operation. When X-ray-to-charge conversion occurs in the photoconductor, a charge packet drifts toward the input pad of the unit pixel. Then, the charge preamplifier generates a voltage signal proportional to the received charge amount, and the voltage signal is compared with a voltage threshold (V_{TH}) which represents the pre-defined energy level so as to detect an input of sufficient amplitude. If the voltage (V_{OUT}) is larger than the threshold (V_{TH}), the comparator triggers the photon counter for increment by 1. The cumulative value of the counter represents the number of photons received at the pixel. Finally, a grayscale X-ray image is generated by the total data gathered from all the pixels.

In the design of a high performance X-ray image detector, several requirements and restrictions must be satisfied. In the imager chip, the electrical power available per pixel is usually restricted due to the potentially high number of pixels. Moreover, each X-ray photon generates a small charge amount with a typical range of 1–10 ke^-; low-noise and high charge-to-voltage conversion gain are therefore required for the detector pixel to achieve adequate charge sensitivity. In addition, a small semiconductor area per pixel is important, because small pixel size enhances the spatial resolution of the X-ray image. Increased pixel-to-pixel uniformity is also required for improved image quality.

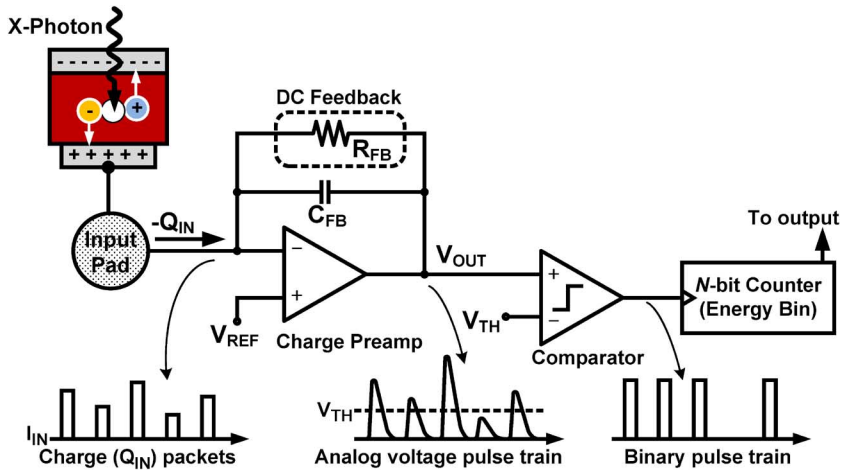

Fig. 3. Conventional direct X-ray photon-counting pixel topology.

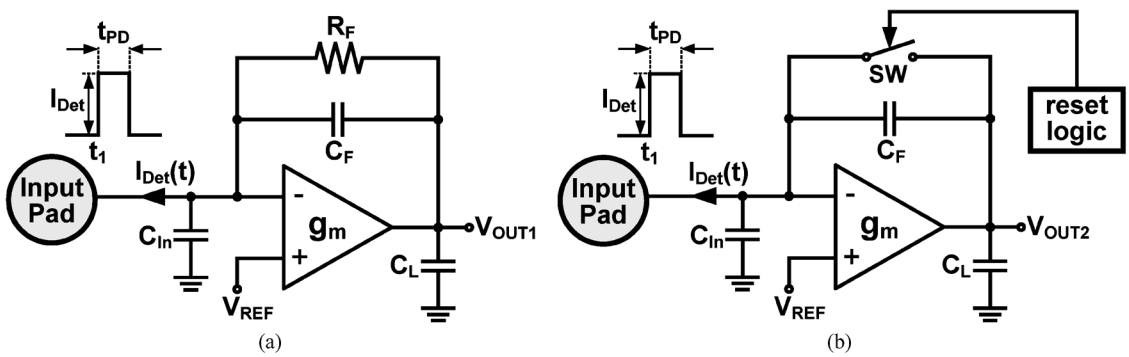

Fig. 4. Circuit topology: (a) DC-feedback charge preamplifier; (b) proposed sampling-based charge preamplifier.

Several efforts to develop high performance X-ray photon counting imager ICs have been reported. A photon counting IC with 256 × 256 pixels with a pixel pitch of 55-μm was presented in [5]. However, this chip is capable of identifying only a single energy band. An improved version of [5] was proposed in [6] and [7]. In this chip, a 55-μm single pixel could recognize dual energy band of the photon. Another 32 × 32 pixels photon-counting chip [8] also made it possible to obtain dual-energy X-ray images with a high dynamic range. In addition, it has the functionality of reducing the comparator threshold dispersion in each pixel. However, its pixel size of $200 \times 200\ \mu\mathrm{m}^2$ is much larger than that of other designs and thus results in low spatial resolution. A triple-energy imaging chip using three comparators in a pixel with a pixel pitch of 109-μm was reported in [9]. Several other chips [10]–[12] can also be found in the literature, and they are similar to those mentioned above.

In this paper, we present an asynchronous sampling-based 128 × 128 direct photon counting X-ray image detector with a $\mathrm{HgI_2}$ photoconductor for high quality multispectral X-ray medical imaging. In the photon counting pixel, the proposed sampling-based charge preamplifier operates with high charge-to-voltage conversion gain ($107\ \mathrm{mV/ke^-}$) and a fast hard-reset scheme. It also reduces threshold dispersion and electronic noise. In addition, we present a compact in-pixel ADC that discriminates three energy levels of a single X-ray photon with only a single comparator. The proposed chip achieves high spatial resolution ($60 \times 60\ \mu\mathrm{m}^2/\mathrm{pixel}$) and low power consumption ($4.6\ \mu\mathrm{W/pixel}$).

II. Sampling-Based Charge Preamplication

Every pixel of an X-ray image detector contains a charge preamplifier that converts the collected charge packets into voltage pulses. Fig. 4(a) shows the charge preamplifier that is used in most conventional X-ray image detectors (as shown in Fig. 3) with parasitic capacitances. It consists of an operational transconductance amplifier (OTA), a feedback capacitor C_{F}, and a resistor R_{F} for DC feedback. The input parasitic capacitance C_{In} is the sum of the sensing element capacitance and the OTA input capacitance. The load capacitance C_{L} is on the output of the OTA. Due to the virtual short at the input of the OTA, the pulse of an input charge from a sensing element, $I_{\mathrm{Det}}(t)$, is transferred onto the feedback capacitor, C_{F}, and creates a step of output voltage, V_{OUT1}. In order to achieve high charge-to-voltage conversion gain, R_{F} should be as large as possible to prevent charge loss through it. Usually, a feedback resistor R_{F} in the $\mathrm{M\Omega - G\Omega}$ range is required as a DC-feedback element; however it is not easy to implement such a high valued resistor in monolithic processes. Therefore, the DC-feedback charge preamplifier requires a circuit [13] that behaves like a large resistor. However, this DC feedback circuit is very sensitive to process-voltage-temperature (PVT) variation due

to the use of sub-nA current bias; it leads to undesirable offset voltage and variable discharge time. Moreover, a large $R_{\rm F}$ makes it difficult for the $C_{\rm F}$ to discharge completely before the next charge packet arrives due to the increased time-constant, $R_{\rm F}C_{\rm F}$. This degrades the maximum available processing rate of the detector pixel. Consequently, the charge-to-voltage conversion efficiency and the charge reset speed are in a trade-off relationship because of the DC-feedback with $R_{\rm F}$.

To solve this trade-off problem between the conversion gain and reset time, we propose a sampling-based charge preamplifier, as shown in Fig. 4(b). Instead of the feedback resistor $R_{\rm F}$, the sampling-based preamplifier uses a switch, SW, to completely discharge the feedback capacitor $C_{\rm F}$ in a short time (hard reset). Before the charge packet is sampled, $C_{\rm F}$ is reset by SW for a short time duration. When the preamplifier samples the charge packet, $I_{\rm Det}(t)$, the SW is off, and the pulse of the charge packet is then quickly converted into output voltage $V_{\rm OUT2}$ without loss, and $V_{\rm OUT2}$ stays at its peak value until the SW resets $C_{\rm F}$. After the voltage pulse processing, the feedback analog switch is turned on by the reset control logic, and then the charge reset is performed immediately within a very short period.

The proposed sampling-based architecture has a similar architecture to that for the time-variant approach, which is often used in synchronous applications for high frame rate processing [14]–[16]. In this application, however, the synchronous time-variant approach can lead to dead time, during which signal charge pulses are destroyed without being detected. In order to detect asynchronous charge pulses without dead time, we present a sampling-based charge preamplifier in conjunction with an asynchronous self-reset control logic in this paper.

In the following, we discuss the advantages of the proposed sampling-based charge preamplifier in comparison with the conventional DC-feedback preamplifier. Assuming that the OTA shown in Fig. 4 is a single-stage amplifier with infinite output impedance, the transimpedance function $Z_1(s)$ of the conventional charge preamplifier in Fig. 4(a), is given by (1), and the transimpedance function $Z_2(s)$ of the proposed sampling-based charge preamplifier in Fig. 4(b) is given by (2). (See the equations at the bottom of the page.) The transimpedance function $Z_1(s)$ possesses dominant and non-dominant poles at $1/R_{\rm F}C_{\rm F}$ and $g_{\rm m}/(C_{\rm L}+C_{\rm In}+C_{\rm L}C_{\rm In}/C_{\rm F})$, respectively. The high frequency zero at $g_{\rm m}/C_{\rm F}$ is usually negligible. For sufficiently high transconductance $g_{\rm m}$ of OTA, (1) and (2) can be approximated as (3) and (4), respectively.

$$Z_1(s) = \frac{R_F}{1+sR_FC_F} \tag{3}$$

$$Z_2(s) = \frac{1}{sC_F} \tag{4}$$

Suppose an input charge pulse $I_{\rm Det}(t)$ is equal to $I_{\rm Det}\cdot u(t-t_1) - I_{\rm Det}\cdot u(t-t_1-t_{\rm PD})$, where t_1 is the starting time of the $I_{\rm Det}$ current pulse; and $t_{\rm PD}$ is the current pulse duration. Thus, the pulse of a charge packet $Q_{\rm Det}$ is equal to $I_{\rm Det}\cdot t_{\rm PD}$. By the inverse Laplace transforms of (3) and (4), at the end of an input current pulse ($t = t_1 + t_{\rm PD}$), the output voltage $V_{\rm OUT1}$ of Fig. 4(a) and $V_{\rm OUT2}$ of Fig. 4(b) can be expressed as (5) and (6), respectively.

$$V_{OUT1}(t_1+t_{PD}) = R_F\frac{Q_{Det}}{t_{PD}}\left(1-e^{-\frac{t_{PD}}{C_FR_F}}\right) \tag{5}$$

$$V_{OUT2}(t_1+t_{PD}) = \frac{1}{C_F}\int_{t_1}^{t_1+t_{PD}} I_{Det}(t)\cdot dt = \frac{Q_{Det}}{C_F} \tag{6}$$

By using a Taylor series expansion, (5) can be separated into two parts: the charge-to-voltage conversion term through the feedback capacitor $C_{\rm F}$ and the error term due to the feedback resistor $R_{\rm F}$, as described in (7).

$$\begin{aligned} V_{OUT1}(t_1+t_{PD}) &= R_F\frac{Q_{Det}}{t_{PD}}\left[1-\sum_{n=0}^{\infty}\frac{1}{n!}\left(-\frac{t_{PD}}{C_FR_F}\right)^n\right] \\ &= \frac{Q_{Det}}{C_F} - \frac{R_FQ_{Det}}{t_{PD}}\sum_{n=2}^{\infty}\frac{1}{n!}\left(-\frac{t_{PD}}{C_FR_F}\right)^n \end{aligned} \tag{7}$$

Therefore, the charge-to-voltage conversion gains of Fig. 4(a) and Fig. 4(b) can be defined as (8) and (9), respectively. The second term on the right side of (8) is the gain error due to the resistive DC-feedback. According to the above analysis, the proposed sampling-based charge preamplifier converts the input charge pulse into a voltage signal without loss; hence the gain of the sampling-based preamplifier can be designed to be much higher than that of the conventional DC-feedback preamplifier.

$$\frac{V_{OUT1}}{Q_{Det}} = \frac{1}{C_F} - \frac{R_F}{t_{PD}}\sum_{n=2}^{\infty}\frac{1}{n!}\left(-\frac{t_{PD}}{C_FR_F}\right)^n \tag{8}$$

$$\begin{aligned} \frac{V_{OUT1}}{I_{Det}}(s) &= Z_1(s) \\ &= \frac{R_F(1-sC_F/g_m)}{1+s\left(R_FC_F+\frac{C_L+C_{In}}{g_m}\right)+s^2(C_LC_{In}+C_LC_F+C_{In}C_F)\frac{R_F}{g_m}} \end{aligned} \tag{1}$$

$$\begin{aligned} \frac{V_{OUT2}}{I_{Det}}(s) &= Z_2(s) \\ &= \frac{1-sC_F/g_m}{sC_F+s^2\frac{C_LC_{In}+C_LC_F+C_{In}C_F}{g_m}} \end{aligned} \tag{2}$$

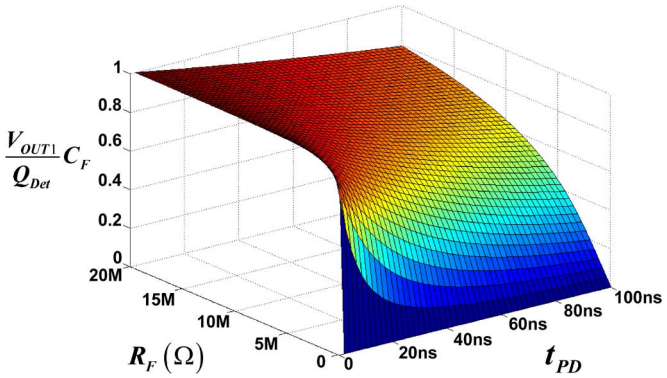

Fig. 5. Calculated charge-to-voltage conversion efficiency ($= V_{\mathrm{OUT1}}/V_{\mathrm{OUT2}}$) depending on the feedback resistor R_{F} and on the input current pulse duration t_{PD} for $C_{\mathrm{F}} = 10$ fF and $Q_{\mathrm{Det}} = 0.5$ fC in Fig. 4(a).

$$\frac{V_{OUT2}}{Q_{Det}} = \frac{1}{C_F} \tag{9}$$

Examining (8), we see that the gain error term is dependent on the feedback resistor R_{F} and the duration period of the input current pulse, t_{PD}. Fig. 5 shows the calculated charge-to-voltage conversion efficiency ($= V_{\mathrm{OUT1}}/V_{\mathrm{OUT2}}$) in relation to R_{F} and t_{PD}. As seen in Fig. 5, the longer t_{PD} is, the larger the contribution of the gain error of V_{OUT1} is. In addition, the feedback resistor R_{F} must be increased to enhance the conversion efficiency. However, the charge reset time, which is proportional to the decay time of $R_{\mathrm{F}}C_{\mathrm{F}}$, is also increased by large R_{F}. Longer charge reset time limits the maximum photon counting rate available per pixel. Furthermore, as can be seen in (8), if t_{PD} varies randomly or depends on the amount of Q_{Det}, the charge-to-voltage conversion gain is likely to be non-linear. In contrast, in the proposed sampling-based charge preamplifier, there is no loss in charge-to-voltage conversion, and the charge-to-voltage conversion is highly linear regardless of t_{PD}, as described in (9). For comparison, Fig. 6 shows the outputs of simulated preamplifiers to an input charge packet of 0.5 fC for the conventional DC-feedback preamplifier responses with R_{F} sweep and the proposed sampling-based preamplifier response.

The main difference between the two architectural solutions is the existence of the DC feedback resistance. The principal noise source in the feedback resistor is thermal noise. The power spectral density (PSD) $S_{\mathrm{N,F}}$ of the thermal voltage noise on the charge preamplifier's output contributed by the feedback resistor can be expressed in (10), shown at the bottom of the page. Note that the poles of the feedback resistor noise PSD are equal to the poles of the signal transimpedance function of (1). Therefore, the equivalent noise charge $ENC_{\mathrm{N,F}}$, as given in (11), can be approximated by the integral of a first-order noise voltage PSD at a bandwidth defined by the dominant pole, divided by the charge-to-voltage conversion factor.

$$ENC_{N,F} \approx \sqrt{kTC_F} \tag{11}$$

The thermal noise of the OTA also affects the noise performance of the charge preamplifier. The major component of the thermal noise in a well-designed OTA is contributed by the input transistors. The output noise PSD $S_{\mathrm{N,A}}$, as given by (12), is found from a simplified analysis, neglecting the noise of the remaining transistors. Using (12), a simple approximation of the amplifier $ENC_{\mathrm{N,A}}$ can be achieved, as given by (13). (See the equations at the bottom of the page.) According to (11) and (13), a value of the feedback resistor has no influence on the ENC, because opposite effects of the resistor simultaneously affect the spectral density and the bandwidth. Therefore, there is no difference between the two architectural solutions in terms of thermal noise effects depending on the existence of the feedback resistor.

Another significant noise is DC leakage current flowing to the detector pixel from the photoconductor. In the conventional structure of Fig. 4(a), the DC leakage current flows across the DC feedback resistor and creates a DC offset voltage in the charge preamplifier output. To cope with leakage current in the DC-feedback preamplifier, an effective solution was reported in [13]. In the proposed sampling-based architecture of Fig. 4(b), the asynchronous behavior of the charge reset due to the randomness of the process of charge packet arrivals causes variable integration of the leakage current, which leads to a variable offset voltage on the preamplifier output. In order to minimize this effect in the proposed sampling-based architecture, the

$$S_{N,F}(s) = \frac{4kTR_F|1 + sC_{In}/g_m|^2}{\left|1 + s\left(R_FC_F + \frac{C_L+C_{In}}{g_m}\right) + s^2(C_LC_{In} + C_LC_F + C_{In}C_F)\frac{R_F}{g_m}\right|^2} \tag{10}$$

$$S_{N,A}(s) = \frac{(4kT/g_m)\,|1 + sR_F(C_{In} + C_F)|^2}{\left|1 + s\left(R_FC_F + \frac{C_L+C_{In}}{g_m}\right) + s^2(C_LC_{In} + C_LC_F + C_{In}C_F)\frac{R_F}{g_m}\right|^2} \tag{12}$$

$$ENC_{N,A} \approx \sqrt{kT\frac{C_FC_{In}}{C_L}} \tag{13}$$

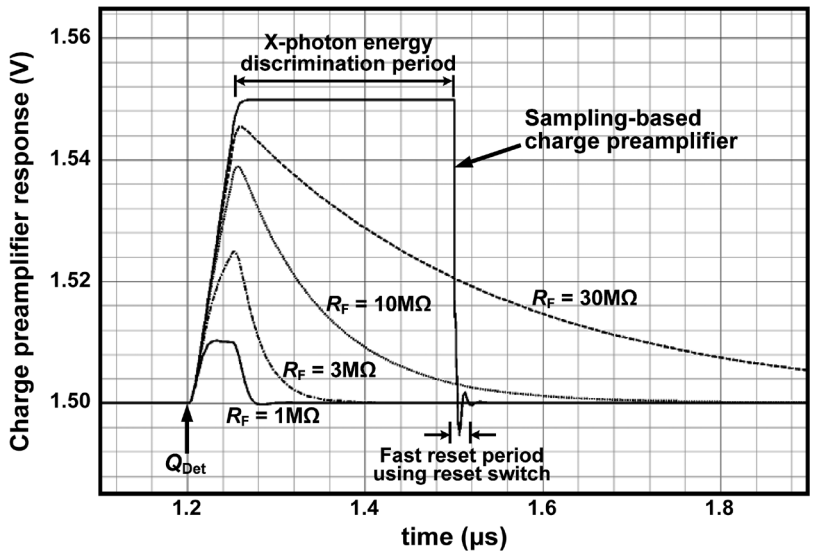

Fig. 6. Simulated DC-feedback and proposed sampling-based charge preamplifier responses to an input charge packet of 0.5 fC for $t_{\rm PD} = 50$ ns, $C_{\rm F} = 10$ fF, $C_{\rm In} = 90$ fF, $C_{\rm L} = 40$ fF, $g_{\rm m}$ of OTA $= 50$ μS, and open-loop gain of OTA $= 70$ dB.

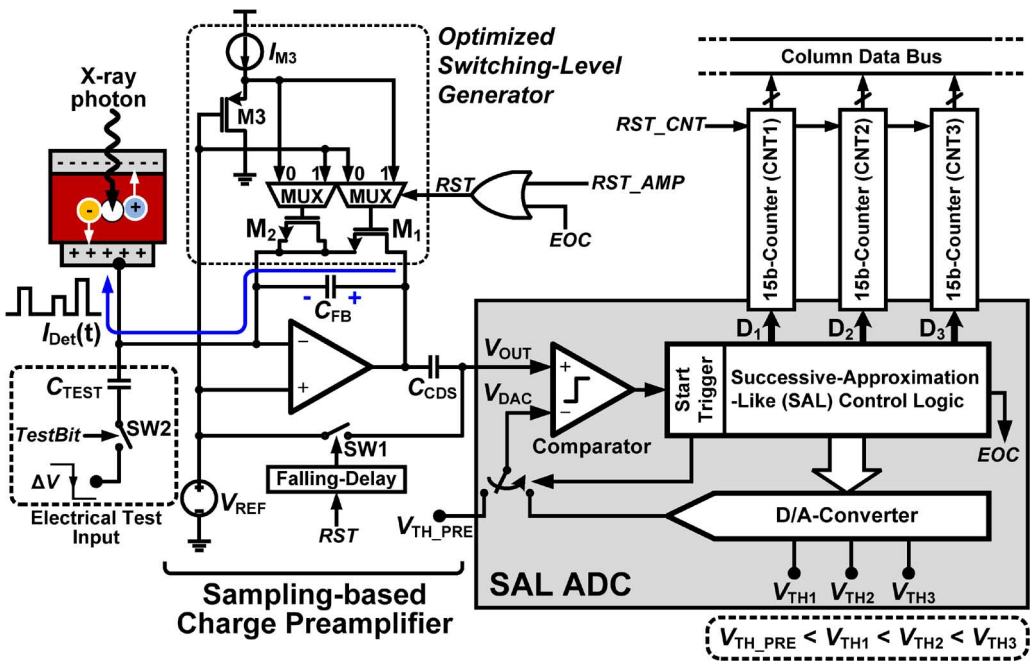

Fig. 7. Detailed schematic of the proposed X-ray photon-counting pixel circuit.

asynchronous self-reset control logic with the preliminary threshold $(V_{\rm TH\_PRE})$ significantly reduces the variable offset voltage. This function will be discussed in detail in Section III-D.

III. Proposed Asynchronous Sampling-Based Multi-Energy Photon Counting Pixel

A. Operational Principle and Structure of Pixel Circuit

Fig. 7 shows the detailed schematic of the proposed X-ray photon-counting pixel circuit, which consists of the proposed sampling-based charge preamplifier, a pixel-level ADC with a start trigger, and three 15-bit counters. As explained in the previous section, the charge preamplifier is designed to acquire electrical charge pulses $I_{\rm Det}(t)$ created by the absorption of the X-ray photons in the photoconductor. The measurement of X-ray photon energy is performed by quantization of the preamplifier output amplitude, which is proportional to the charge packet; hence, the effective energy resolution depends on the accuracy of the charge measurement. The following multi-energy discriminator (pixel-level ADC) classifies the energy of the incoming charge packet into three energy bins. The resultant output pulses ($\rm D_1$, $\rm D_2$, and $\rm D_3$) from the ADC trigger the subordinate three 15-bit counters to count the energy-discriminated X-ray photons. After the energy discrimination period is finished, the ADC activates an asynchronous self-reset signal that represents end-of-conversion (EOC), and $C_{\rm FB}$ is then reset quickly by the reset switch $\rm M_1$ in order to prepare the following charge packet detection. This fast reset enhances the photon

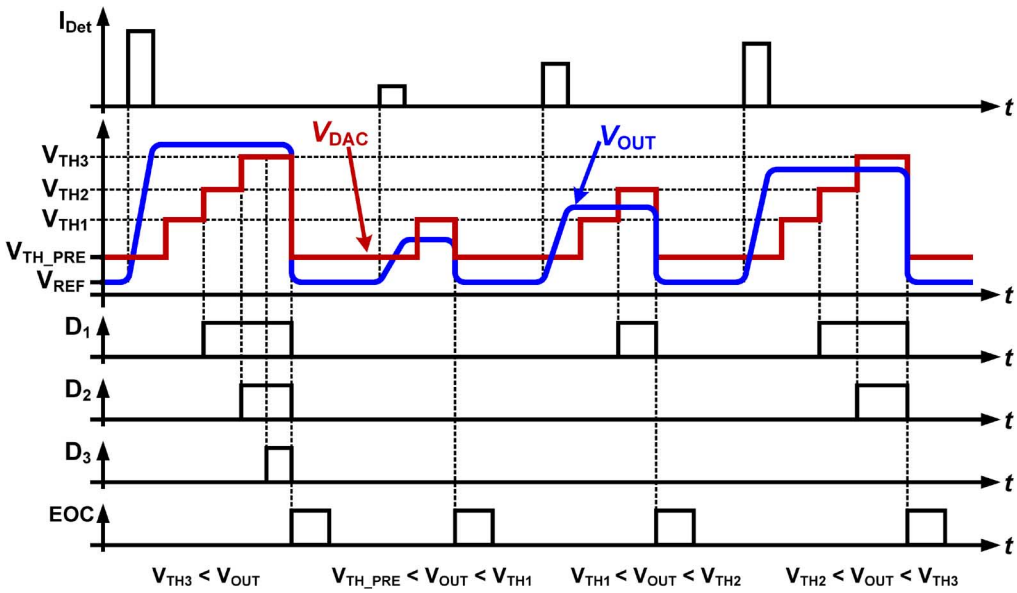

Fig. 8. Example of waveforms in the proposed pixel.

counting rate. Note that the discrimination period must be designed to be shorter than the minimum input charge period so as to avoid charge pulse pile-up from consecutive input charge pulses [17]. Fig. 8 also describes the detailed operational procedure of the proposed photon counting pixel with an example of waveforms.

In order to obtain very sensitive charge detection capability, a small feedback capacitor C_{FB} of 1.5 fF was chosen, which corresponds to a charge-to-voltage conversion gain of 107 $\mathrm{mV}/\mathrm{ke}^{-}$. Increased sensitivity at low X-ray energy not only provides a high contrast ratio but also makes it possible to reduce the radiation dosage and thus lower the damage to patients. This small feedback capacitor C_{FB} is implemented by four 6-fF MIM capacitors connected in series to reduce the pixel-to-pixel gain dispersion. The noise of the detector pixel and the pixel-to-pixel effective threshold mismatch can also affect the charge detection sensitivity. Thus, in the proposed detector pixel, the correlated double sampling (CDS) technique is used to reduce these effects.

B. Optimized Switching-Level Generator

Since the feedback capacitance C_{FB} is very small, charge-injection from the reset switch M_1 must be kept as small as possible. To solve this problem, we propose an optimized switching-level generator in conjunction with the dummy switch M_2. Before describing the proposed optimized switching-level generator, the charge injection from the analog MOS switch is briefly reviewed. Fig. 9 shows the simulated waveform of the released channel charge current $I_{\mathrm{Ch}}(t)$ from the switch in the turn-off transition. In order to observe the injected charge amount, a falling ramp is applied to the gate voltage V_{G} of the analog switch. Some important facts of the charge injection in a MOS switch can be observed from the waveform of the current $I_{\mathrm{Ch}}(t)$. As depicted in Fig. 9, the area under the curve of the current $I_{\mathrm{Ch}}(t)$ during the turn-off transition can be separated into three different components Q_{a}, Q_{b}, and Q_{c}, where Q_{a} represents a portion of the channel charges in strong inversion; Q_{b} represents the channel charges in weak inversion; and Q_{c} represents the charges coupled through the gate-to-drain-source overlap capacitance. Because the channel charges in strong inversion, Q_{a}, occupy a large portion of the charge injection, the charge injection will be significantly reduced if the switch operates in the weak inversion region. More detailed analyses of the weak inversion charge injection in an analog switch can be found in [18], [19].

Instead of using the conventional VDD-to-GND switching, the proposed optimized switching-level generator turns the analog switch on and off only in the weak inversion region. In order to turn the switch on in weak inversion, the optimized switching-level generator generates nearly-minimum gate voltage V_{G}; consequently, the V_{GS} of the reset switch is close to the MOS threshold V_{th} during the turn-on phase. When the analog switch turns off, the V_{GS} of the switch is effectively zero. As a result of using the optimized switching-level generator, the area under the curve of the current $I_{\mathrm{Ch}}(t)$ in the turn-off transition of $t_1 < t < t_4$ can be reduced to the channel charges in the weak inversion region ($t_2 < t < t_3$ in the bottom of Fig. 9); the released channel charges from the switch are reduced more than seven-fold compared with the conventional VDD-to-GND switching. Therefore, the proposed optimized switching-level generator significantly reduces charge injection from the analog switch.

Fig. 10 shows the schematic of the proposed the optimized switching-level generator circuit. The circuit is composed of a source follower M_3, current source I_{M3}, and analog MUXs. During the reset phase of the charge preamplifier, $V_{\mathrm{GS,M3}} + V_{\mathrm{REF}}$ is applied to the gate of the reset switch M_1, and $V_{\mathrm{GS,M1}}$ of the reset switch is thus equal to $V_{\mathrm{SG,M3}}$. However, an exceedingly small $V_{\mathrm{GS,M3}}$ ($= V_{\mathrm{GS,M1}}$ during the reset-on phase)

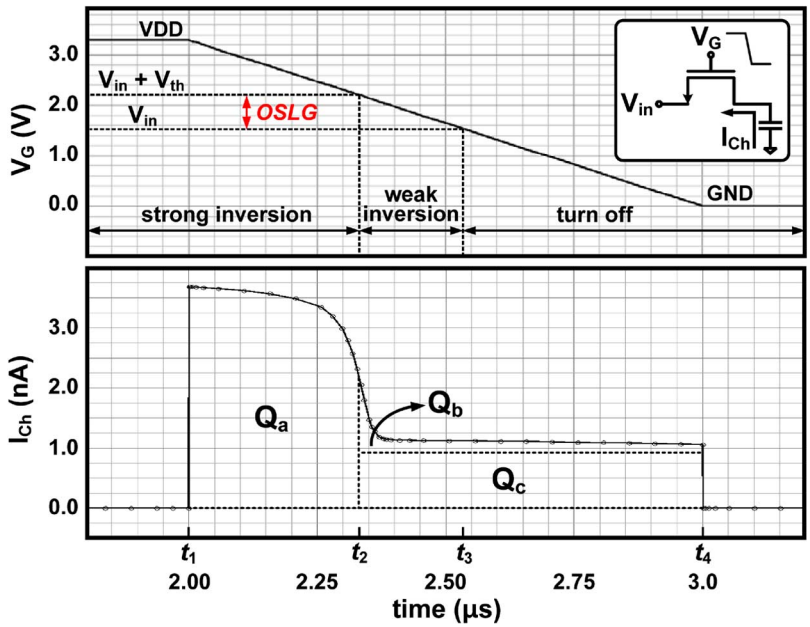

Fig. 9. Simulated waveforms of the voltage ($V_{\rm G}$) at the gate of the analog switch and the current $I_{\rm Ch}$ due to charge injection from the switch in turn-off transition. The width and length of the NMOS switch are 600 nm and 350 nm, respectively.

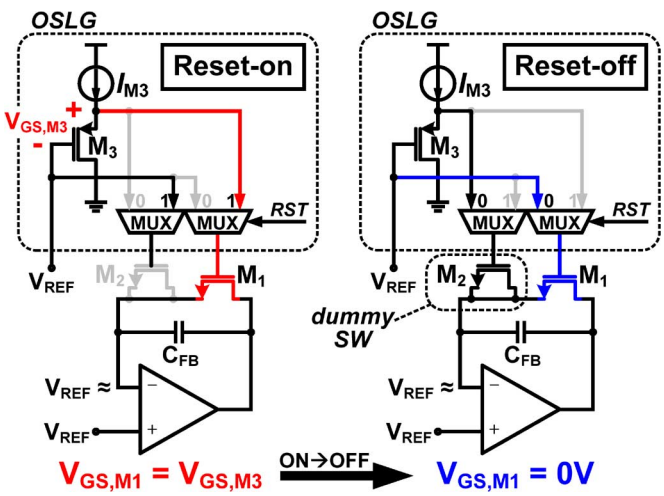

Fig. 10. Schematic of the proposed optimized switching level generator (OSLG) for minimizing charge injection from the switch $\rm M_1$.

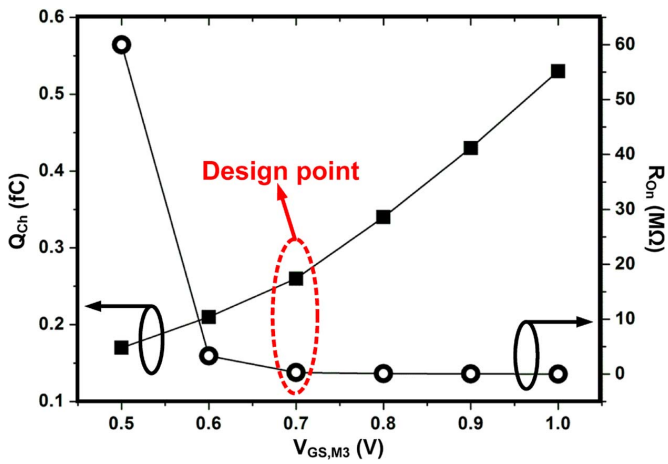

Fig. 11. Simulation results: the released channel charge ($Q_{\rm Ch}$) of the switch $\rm M_1$ in turn-off transition and the on-resistance ($R_{\rm On}$) of the switch $\rm M_1$ during the turn-on phase. The threshold voltage of NMOS transistor $\rm M_1$ is approximately 680 mV.

increases the on-resistance of the switch $\rm M_1$. This leads to a reduction of the charge reset speed of the sampling-based charge preamplifier. By adjusting $I_{\rm M3}$, the voltage $V_{\rm GS,M1}$ can be controlled during the reset phase. After the reset phase, the reset switch $\rm M_1$ is turned off with $V_{\rm GS,M1} = 0$ V by applying $V_{\rm REF}$ to the gate of $\rm M_1$. At the same time, the dummy switch $\rm M_2$ is turned on to cancel the charge injection from $\rm M_1$. Fig. 11 presents the simulation results of the released channel charge ($Q_{\rm Ch}$) of $\rm M_1$ at the turn-off transition and the on-resistance ($R_{\rm On}$) of $\rm M_1$ during the turn-on phase for $V_{\rm GS,M3}$ sweep from 0.5 V to 1 V. As seen in Fig. 11, lowering of $V_{\rm GS,M3}$ in the optimized switching-level generator circuit reduces the charge injection from the switch $\rm M_1$, whereas the on-resistance of $\rm M_1$ increases. In this design, the optimal point of $V_{\rm GS,M3}$ is found to be 0.7 V for both small charge injection and fast charge reset speed. It is seen that the released channel charge $Q_{\rm Ch}$ of 0.26 fC at $V_{\rm GS,M3} = 0.7$ V correlates well with the area under the curve of $I_{\rm Ch}(t)$ of Fig. 9 in the transition of $t_2 < t < t_3$. However, the $V_{\rm GS,M3}$ must be designed to be marginally higher than that of the optimal design point, considering the PVT variations of the optimized switching-level generator circuit. The charge reset speed can be guaranteed by keeping the on-resistance of the switch $\rm M_1$ appropriately small. The increased charge injection effect caused by higher $V_{\rm GS,M3}$ can be easily compensated by the subsequent correlated double sampling (CDS) operation described in the following section.

C. Correlated Double Sampling

While the charge injection from the reset switch is drastically reduced by the optimized switching-level generator, the residual

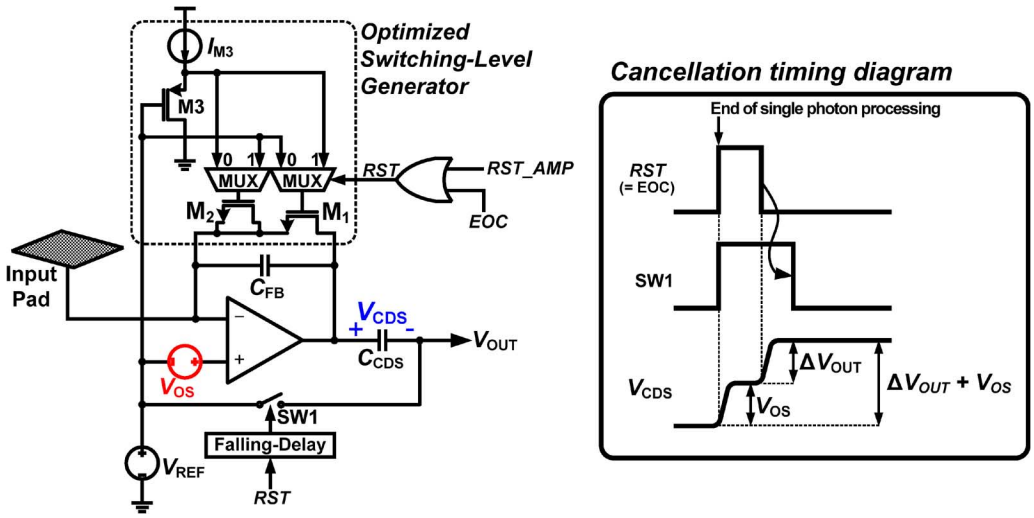

Fig. 12. Switch operations for cancellation of the offset ($V_{\rm OS}$) of OTA and the residual error voltage ($\Delta V_{\rm OUT}$) due to charge-injection from $\rm M_1$.

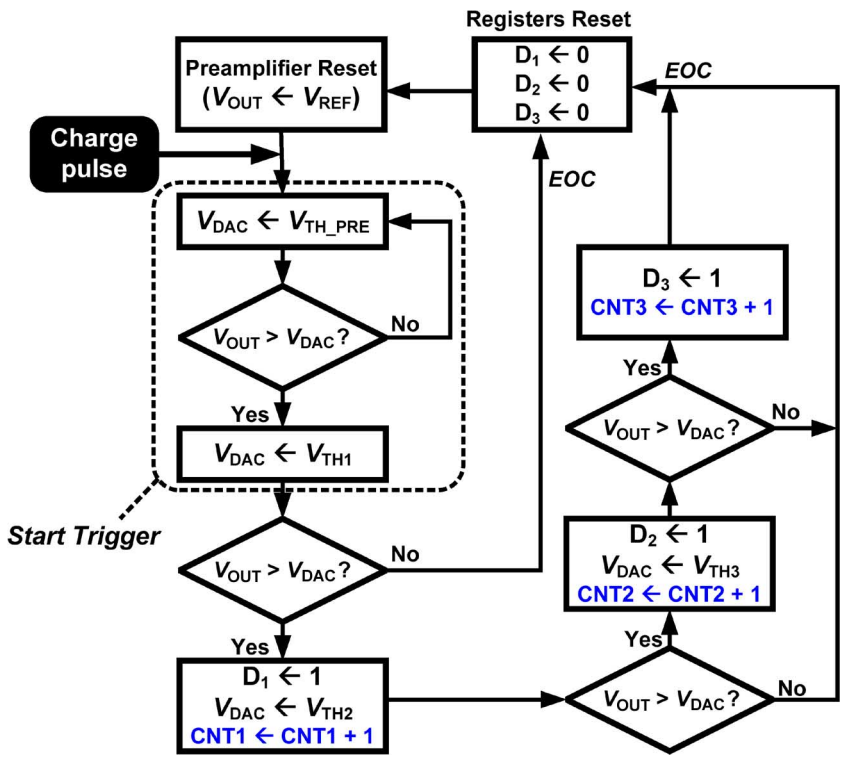

Fig. 13. Proposed successive-approximation-like (SAL) algorithm for X-ray photon energy discrimination.

error $\Delta V_{\rm OUT}$ due to charge injection from $\rm M_1$ still remains on the charge preamplifier output. From our fabricated chips, the remaining error (at the preamplifier output) $\Delta V_{\rm OUT}$ of approximately 3 mV was measured without correlated double sampling. However, the proposed sampling-based operation allows cancellation of not only the residual error $\Delta V_{\rm OUT}$ due to charge injection but also the offset voltage $V_{\rm OS}$ of OTA by using the correlated double sampling (CDS) technique. Fig. 12 describes the proposed error cancellation procedure. Firstly, the offset of the OTA ($V_{\rm OS}$) is sampled by $C_{\rm CDS}$ during the reset phase with switches SW_1 and $\rm M_1$ on. After that, the reset switch $\rm M_1$ turns off, and the residual error voltage ($\Delta V_{\rm OUT}$) due to charge injection from $\rm M_1$ is also stored in $C_{\rm CDS}$. Because $V_{\rm OUT}$ starts from $V_{\rm REF}$ regardless of the stored error amount, those error effects are eliminated at the output. The charge injection from the SW_1 is negligible because $C_{\rm CDS}$ of 65 fF is much higher than $C_{\rm FB}$, and most of the released channel charges from the SW_1 flow to $V_{\rm REF}$ due to the low impedance. Owing to the CDS operation, the offset of the charge preamplifier is suppressed; thus, the pixel-to-pixel uniformity of the pixel array is significantly improved. Note that it is difficult to compensate the OTA's offset in the conventional charge preamplifier with a resistive DC feedback. In addition, the $1/f$ noise reduction also takes place by virtue of the CDS. However, note that the filtering effect of

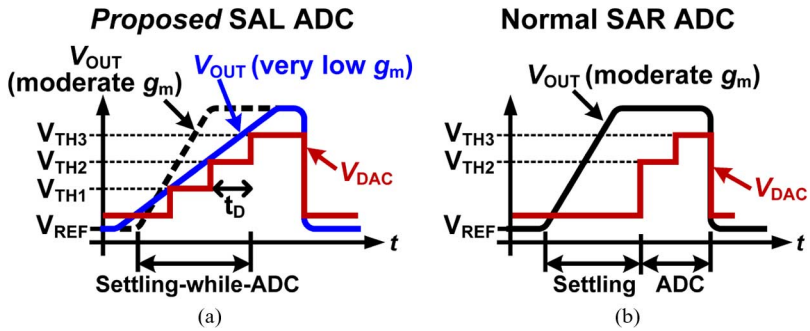

Fig. 14. Charge preamplifier response and internal DAC waveform: (a) proposed SAL ADC (linear search fashion); (b) conventional SAR ADC (binary search fashion).

the $1/f$ noise is expected to be dependent on the asynchronous charge pulse arrivals, unlike the CDS with constant switching period, in the proposed sampling-based operation.

D. Successive-Approximation-Like ADC

After the charge packet is converted into voltage $(V_{\rm OUT})$, the X-ray photon energy discrimination process is performed by the proposed successive-approximation-like (SAL) ADC. In conventional approaches [5]–[11], multiple comparators are used to discriminate X-ray photon energy, as in a flash-type ADC. However, in segmented X-ray image detectors with a large number of pixels, low power consumption and small area are required. In this paper, we present a low-power and compact-sized SAL ADC, which is adequate for in-pixel photon energy discrimination. Fig. 7 shows the proposed SAL ADC, which is composed of a clock-less comparator, SAL control logic, and thermometer-coded DAC. The preliminary threshold $V_{\rm TH\_PRE}$ is set to be slightly higher than $V_{\rm REF}$ in order to prevent noise including dark DC current from triggering the SAL ADC. If $V_{\rm OUT} > V_{\rm TH\_PRE}$, the *Start Trigger* runs the SAL ADC. The ADC has three energy thresholds, $V_{\rm TH1}$, $V_{\rm TH2}$, and $V_{\rm TH3}$ $(V_{\rm TH1} < V_{\rm TH2} < V_{\rm TH3})$, which can be externally selected by software. Once the SAL ADC starts, $V_{\rm OUT}$ is compared with $V_{\rm TH1}$ first. If $V_{\rm OUT} > V_{\rm TH1}$, then $\rm D_1 = 1$ and the corresponding counter (CNT1) is incremented. Further comparisons are performed with $V_{\rm TH2}$ and/or $V_{\rm TH3}$ and counts up the correspondent counters. If $V_{\rm OUT}$ is smaller than a certain threshold or if all the conversions up to $V_{\rm TH3}$ are completed, all the circuits except for the counters return to the initial condition by the asynchronous self-reset signal, named end-of-conversion (EOC). Because of its compact single comparator structure, the SAL ADC could be integrated in small pixel size $(60 \times 60\ \mu{\rm m}^2)$ with low power consumption $(4.6\ \mu{\rm W/pixel})$ while achieving multi-energy photon counting. When a low energy X-ray photon arrives, the proposed SAL ADC completes photon counting rapidly by skipping higher level comparison, differently from the fixed conversion time of typical ADCs. In X-ray imaging, low energy X-ray photons arrive more frequently than high energy photons. Therefore, the proposed SAL ADC is also applicable to higher counting rate X-ray detectors.

Fig. 13 describes the proposed SAL algorithm for discriminating X-ray photon energy. Unlike traditional successive-approximation-register (SAR) ADCs, the proposed SAL ADC controls internal DAC linearly rather than in a binary search fashion. As a result, the preamplifier settling and the discrimination of the X-photon energy can be done simultaneously (settling-while-conversion). Accordingly, the settling time of the preamplifier is sharable with the energy discrimination period, as depicted in Fig. 14(a). By so doing, the photon counting rate can be improved. Furthermore, the static power consumption of the preamplifier is reduced because of the reduced settling requirement of the preamplifier. A more detailed explanation is provided in the following. Since the response time of the charge preamplifier given by (2) is limited by the non-dominant pole, $1/\tau_{\rm P2} \approx g_{\rm m}/(C_{\rm L} + C_{\rm In} + C_{\rm L}C_{\rm In}/C_{\rm F})$, high OTA transconductance $(g_{\rm m})$ is required for fast response in Fig. 4(b). On the other hand, low OTA power consumption is a consequence of the settling-while-conversion scheme in the proposed SAL ADC, because the required $g_{\rm m}$ of OTA can be relaxed. As shown in Fig. 14(a), the OTA's $g_{\rm m}$ can be reduced until the settling slope of the preamplifier is the same as the transition slope of $V_{\rm DAC}$. For settling to within a 0.25% accuracy, $6\tau_{\rm P2}$ has only to be less than $3t_{\rm D}$, where $t_{\rm D}$ is the

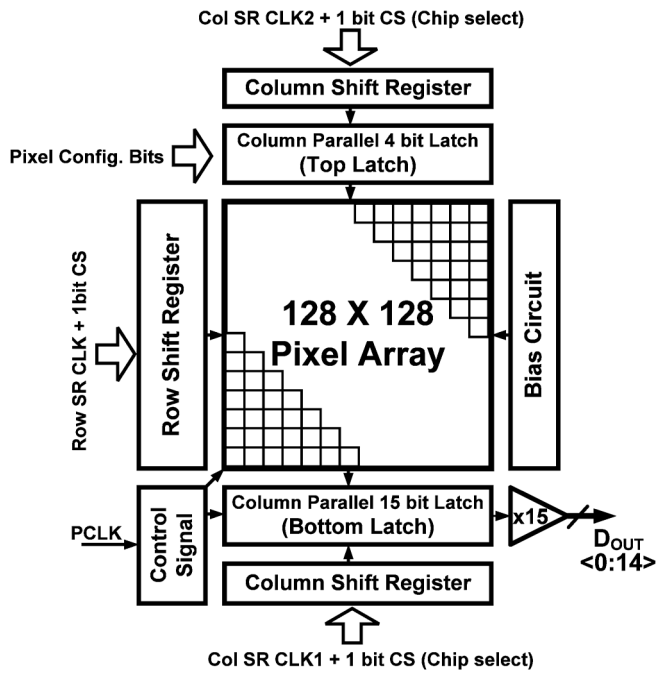

Fig. 15. Full chip architecture.

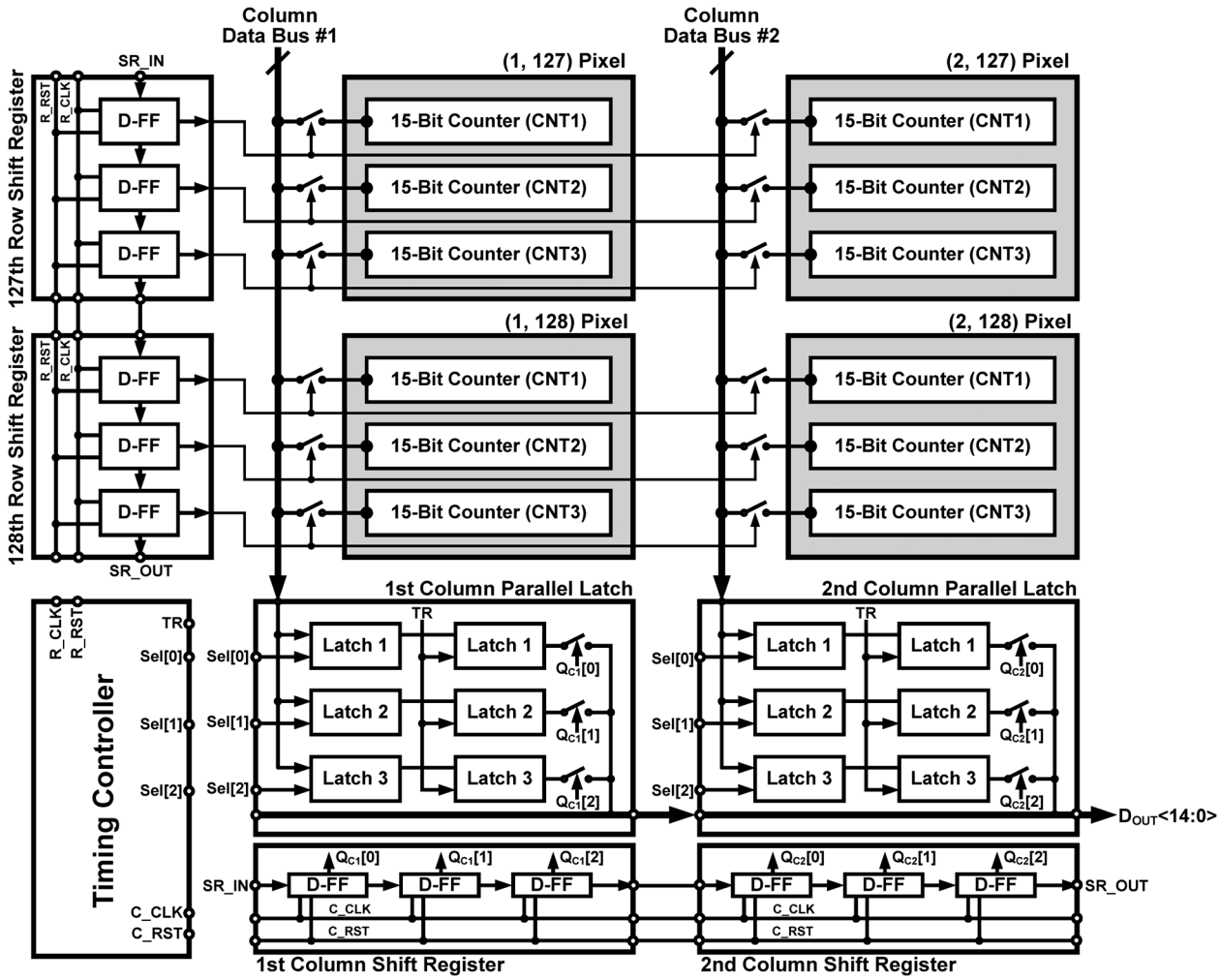

Fig. 16. Pixel-data readout architecture using the column data bus.

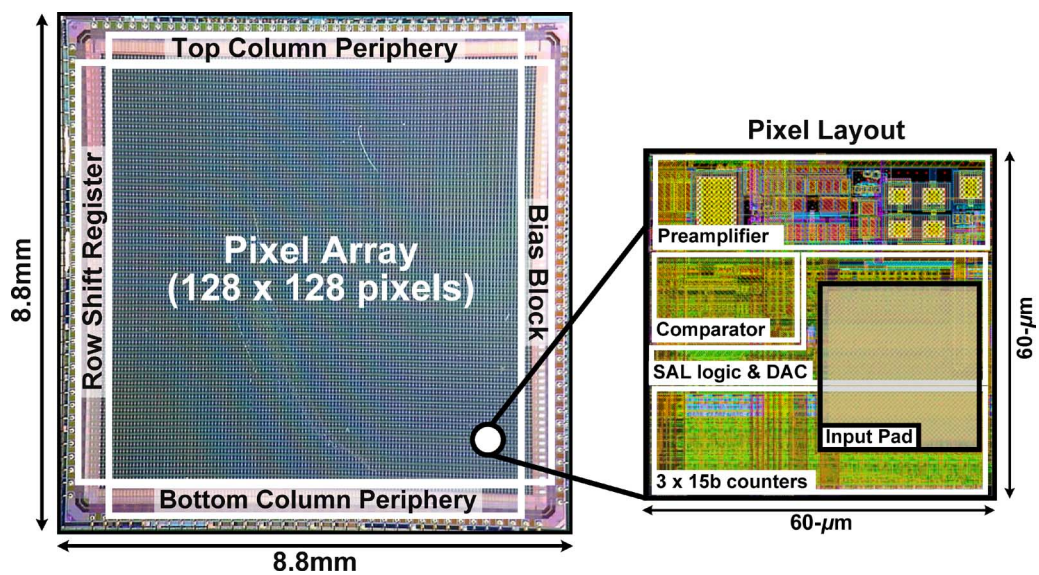

Fig. 17. Chip micrograph and pixel layout [20].

one-step conversion time of the SAL ADC. Therefore, the g_{m} of the OTA can be designed to be reduced as $(C_{\mathrm{L}} + C_{\mathrm{In}} + C_{\mathrm{L}}C_{\mathrm{In}}/C_{\mathrm{F}})/0.5t_{\mathrm{D}}$ by using the proposed settling-while-conversion scheme.

IV. Full Chip Architecture and Pixel-Data Readout

Fig. 15 shows a block diagram of the designed X-ray image detector chip. The charge detecting panel consists of a 128 ×

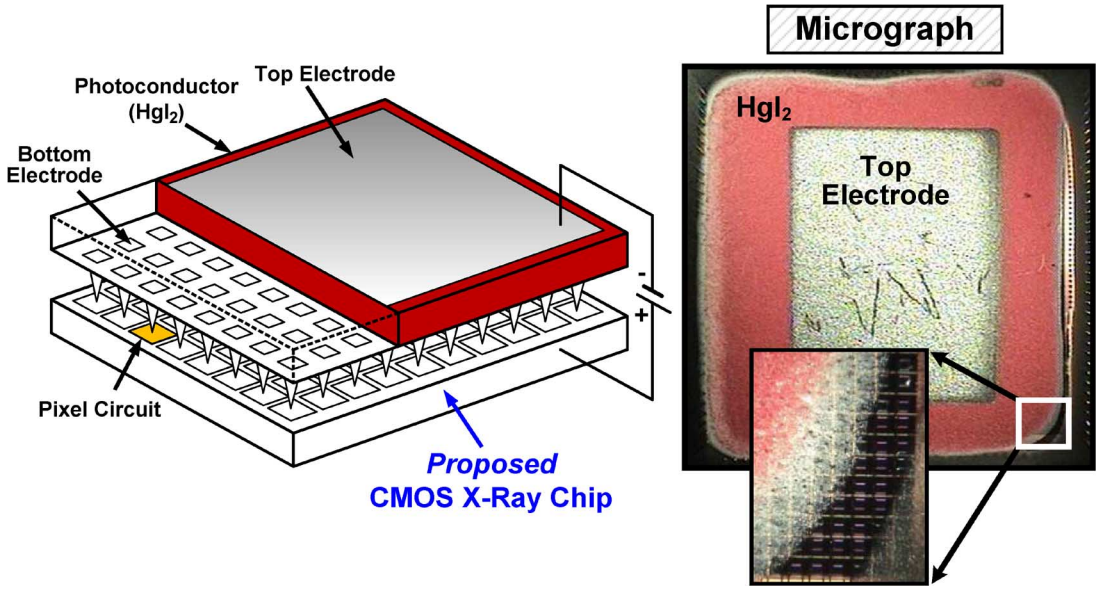

Fig. 18. Implementation of X-ray image detector with photoconductor (HgI_2).

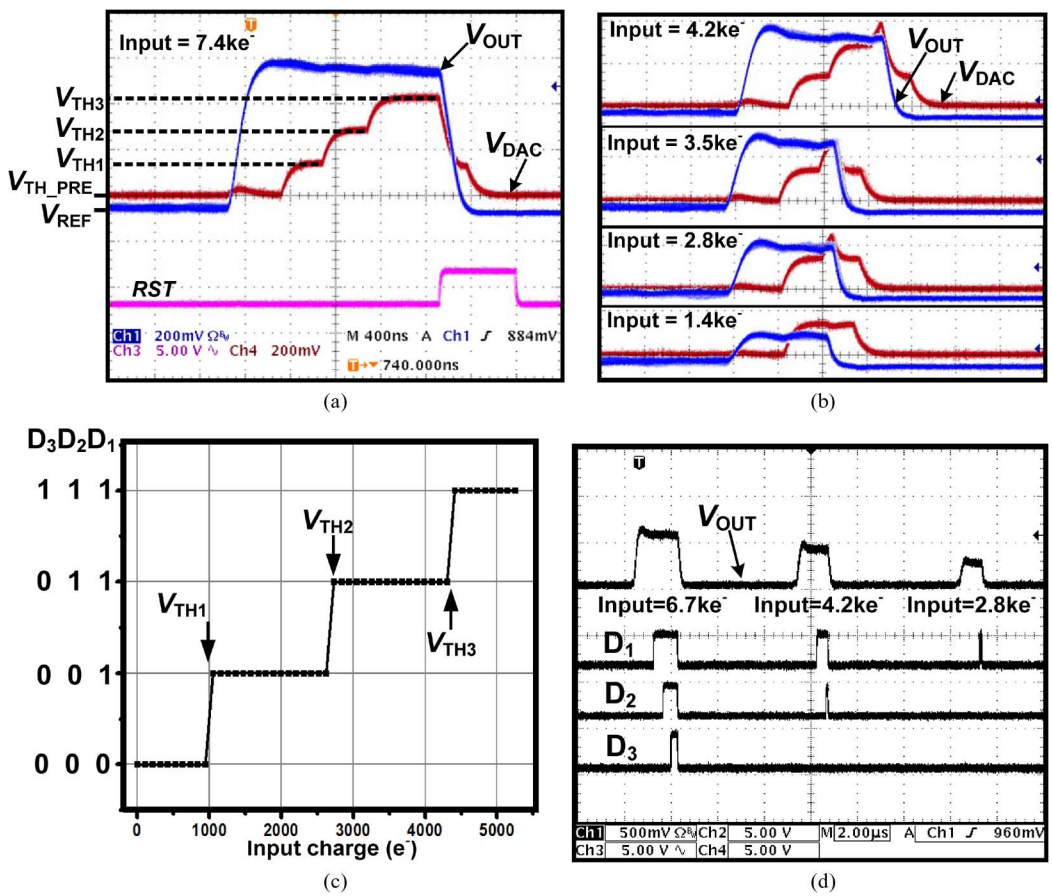

Fig. 19. Pixel measurement results: (a) waveforms of charge preamplifier output and DAC output in SAL ADC; (b) preamplifier and V_{DAC} responses for various levels of input charge pulses; (c) measured transfer function of the SAL ADC; (d) waveforms of energy discrimination results.

128 pixel array with unit pixel size of $60 \times 60\ \mu\mathrm{m}^2$. The pixel array occupies 76.2% of the entire area. The periphery on the right side of the chip contains bias blocks providing the pixel circuit with various bias voltages. Peripheries on the top and bottom are used to write the configuration bits in each pixel and to read the pixel-data, respectively. The left-side shift registers play the role of addressing the pixel array to perform I/O operations. Fig. 16 describes the simplified pixel-data readout structure for the 2×2 pixels located at the bottom-left corner of the chip. The row shift registers transfer the counter data of

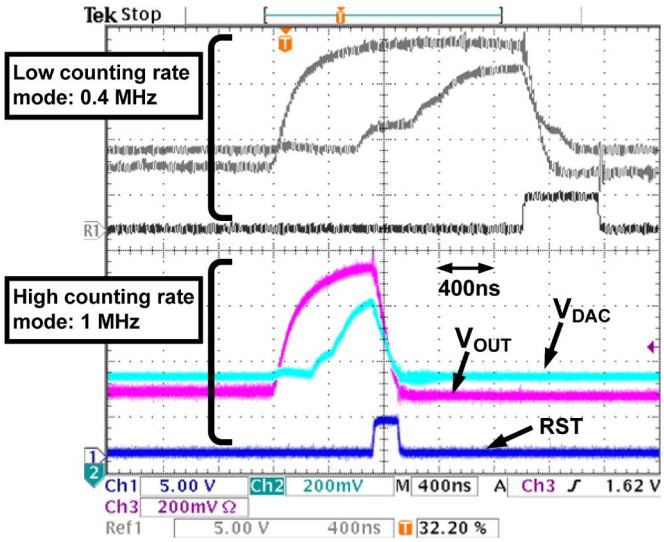

Fig. 20. Measured waveforms of low counting rate mode (0.4 MHz) and high counting rate mode (1 MHz).

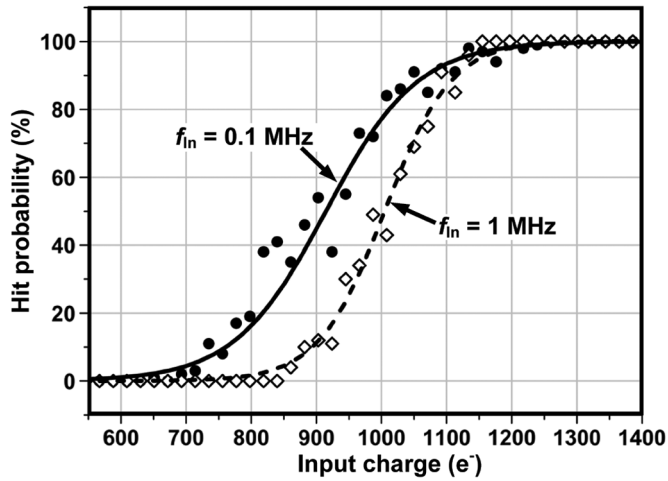

Fig. 21. Measured s-shaped curve of the pixel circuit for evaluating equivalent noise charge (ENC).

each pixel to the column parallel latch located at the bottom periphery via the designated column data bus. Finally, the counter data stored in the column parallel latch are selected by the column shift register and transmitted to the output, $\mathrm{D_{OUT}}\langle 14 : 0\rangle$. Control signals for pixel-data readout are provided by the timing controller. Each row pixel data are stored and transferred to the output in parallel within 60 μs; thus, the pixel-data readout operation is completed within 7.75 ms $(= 60\ \mu\mathrm{s} \times 129)$.

V. Experimental Results

A prototype X-ray photon counting chip was fabricated in a 0.13-μm/0.35-μm 7-metal standard CMOS process [20]. A micrograph of the fabricated chip is shown in Fig. 17. The chip area is 8.8 mm × 8.8 mm including I/O pads. The analog and the digital circuits have been designed to operate with 3.3 V and 1.2 V power supplies, respectively. The fabricated chip contains around 22 million transistors. Fig. 17 shows the detailed layout of a unit pixel, where the pixel pitch is 60 μm. The pixel contains both analog and digital parts. The analog part including the charge preamplifier is located in a deep n-well so that its substrate is separated from the digital switching noise. The input pad for bump bonding to the photoconductor is designed with top metal (Al) and its size is $30 \times 30\ \mu\mathrm{m}^2$. It should be noted that the digital switching noise from the digital circuitry may couple to the charge preamplifier's input via the floating parasitic capacitance formed between the input pad and the underlying digital circuits, and deteriorate the signal integrity. It was verified with parasitic extraction that the floating parasitic capacitance is approximately 26 fF. To avoid this noise coupling problem via parasitic coupling, a shield metal layer biased to AC ground is inserted under the input pad to isolate the noise coupling from the digital switching.

The implementation of the X-ray image detector with a photoconductor is described in Fig. 18. In our implemented system, mercury iodide $(\mathrm{HgI_2})$ is used as a photoconductor material [21]. This photoconductor, $\mathrm{HgI_2}$, is known to have 70 $\mathrm{e^-/keV}$ X-ray-to-charge conversion efficiency. The maximum incoming frequency of the input charge pulses is 0.5 MHz/pixel in our target system. Therefore, the photon counting pixel must finish processing a single X-ray photon within 2 μs. In this implementation, the thickness of the photoconductor is 100 μm.

A. Pixel Measurement Results

Fig. 19 shows the pixel measurement results. Fig. 19(a) shows the transient responses of the charge preamplifier (V_{OUT}) for a 7.4 $\mathrm{ke^-}$ input charge and the corresponding DAC (V_{DAC}) waveforms of the SAL ADC with threshold settings of 2.1 $\mathrm{ke^-}(V_{\mathrm{TH1}})$, 4 $\mathrm{ke^-}(V_{\mathrm{TH2}})$, and 5.5 $\mathrm{ke^-}(V_{\mathrm{TH3}})$. V_{OUT} reaches its peak value within 200 ns and resets to the baseline within 150 ns. Fig. 19(b) shows the charge preamplifier's output, V_{OUT}, and V_{DAC} for various levels of input charge pulses. Note that higher level photon counting is skipped (V_{DAC} does not increase) when the input charge is lower than a certain threshold. Fig. 19(c) shows the measured transfer function of the multi-energy discriminator (SAL ADC) with the input charge sweep at thresholds of 1.15 $\mathrm{ke^-}(V_{\mathrm{TH1}})$, 2.88 $\mathrm{ke^-}(V_{\mathrm{TH2}})$, and 4.6 $\mathrm{ke^-}(V_{\mathrm{TH3}})$, respectively. Fig. 19(d) shows the energy discrimination results ($\mathrm{D_1}$, $\mathrm{D_2}$, and $\mathrm{D_3}$) for three different input charge packets.

The measured maximum photon counting rate of the proposed pixel is 1 MHz, which is sufficiently higher than the maximum charge incoming frequency of 0.5 MHz/pixel. As a result of this design, our X-ray image detector is free from the charge pile-up problem. The photon counting rate can be varied within a range from 0.1 MHz to 1 MHz by adjustment of the digital delay in the SAL controller. Fig. 20 demonstrates several key waveforms at a low counting rate mode (0.4 MHz) and at a high counting rate mode (1 MHz).

The electronic noise of the pixel is measured using the s-shaped curve method [22]. This method gives information on the noise in the entire front-end chain including the preamplifier and comparator circuits. Having a fixed threshold, an input charge is swept from no counter counts (under threshold) condition to 100% hits condition, creating an s-shaped curve.

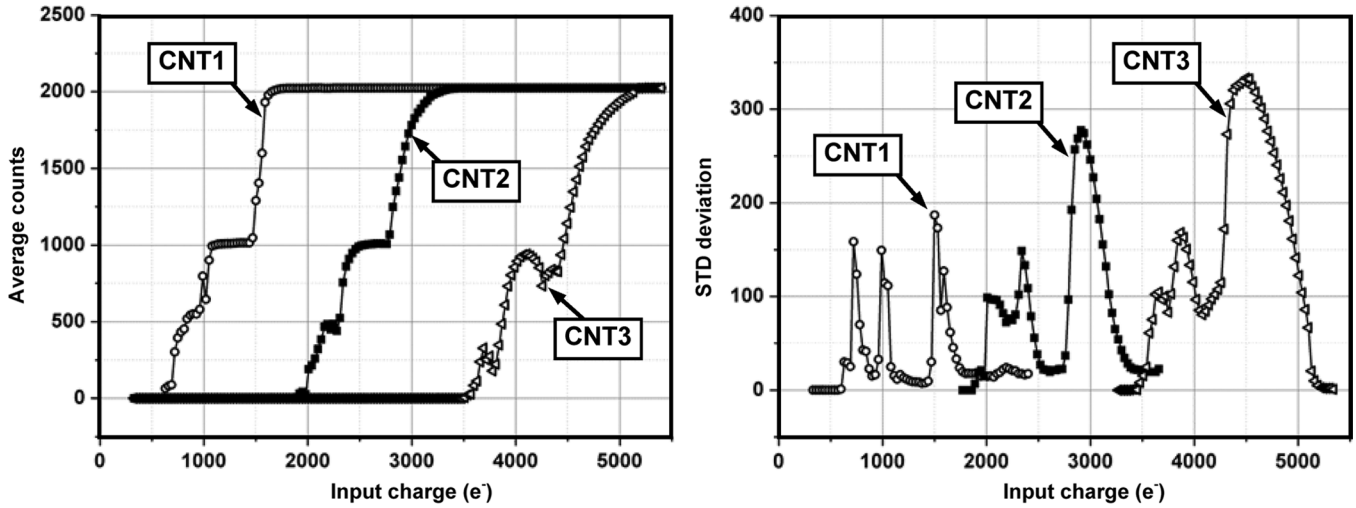

Fig. 22. Measured counted data when 2,000 charge packets are injected: the average and standard deviation of measured counts from total pixels with respect to the amplitude of input charge packet.

The effective threshold is at 50% of this s-curve. The charge difference between the levels of 2% and 98% of the s-curve is four times the R.M.S. noise of the front-end, assuming Gaussian distributed noise. Fig. 21 shows the measured s-curve for our designed pixel. When the frequency $f_{\rm In}$ of the input charge pulse is 0.1 MHz, the transition between 2% and 98% response (4σ) for a single pixel takes place over an equivalent charge variation of 441 $\rm e^-$. Supposing a Gaussian distribution, the measured equivalent noise charge (ENC) at $f_{\rm In} = 0.1$ MHz is 110 $\rm e^-$ rms. On the other hand, the measured ENC at $f_{\rm In} = 1$ MHz is 68 $\rm e^-$ rms. One of the causes of the dependence of ENC on the charge incoming frequency $f_{\rm In}$ is the $1/f$ noise suppression of the proposed sampling-based charge preamplifier. In Fig. 21, some non-monotonicity can be seen due to limited sample numbers and some measurement errors; however, it is still reasonable to estimate the ENC from a fit of the measured s-curve because the minor non-monotonicity in the s-curve has no significant influence on the equivalent charge variation.

In order to measure the minimum detectable energy level of the detector pixel, the energy threshold scanning was performed without any signal at the input, and the measured minimum detectable energy level at which the lowest threshold could be placed was 290 $\rm e^-$.

B. Pixel Array Measurement and X-Radiation Experimental Results

The proposed photon counting X-ray chip contains a total of 16,384 pixels. For evaluating the detector pixel array in the designed X-ray imager, several tests were performed. In order to verify the operation of the energy discrimination with the three 15-bit energy bins (counters) with threshold settings at 1.1 $\rm ke^-(V_{TH1})$, 2.7 $\rm ke^-(V_{TH2})$, and 4.1 $\rm ke^-(V_{TH3})$, 2,000 input charge packets were injected into all pixels by sweeping the amount of charge, and the counts in all pixels were measured. The measured average counts from the total pixels are shown in Fig. 22; the three different energy bands are clearly visible.

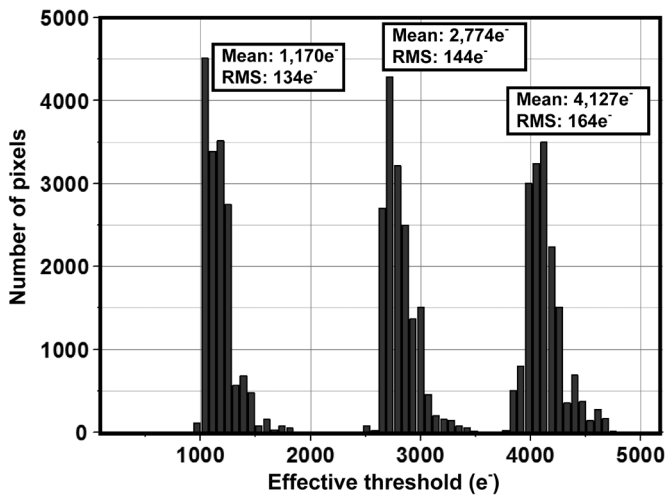

Fig. 23. Measured threshold dispersions for energy thresholds $V_{\rm TH1}$, $V_{\rm TH2}$, and $V_{\rm TH3}$.

As can be seen, there is the non-monotonicity in the average counts of Fig. 22. The global test input port which the electrical test signals are applied to is placed at the top-right of the chip and shared by all pixels. Therefore, due to the interconnection line capacitances and resistances, the responses of the pixels located far from the global test input port can be different from those of the pixels near the global test input port. This structural limitation could have influenced the non-monotonicity of the average counts of Fig. 22. The measured standard deviations in the transition band are also shown in Fig. 22. The deviation of higher energy-level photon counting is slightly worse than that of lower energy-level counting because noise is accumulated due to the chain structure of the SAL controller.

The threshold dispersion is the standard deviation of the effective thresholds of all pixels; it also represents the pixel-to-pixel uniformity. Fig. 23 shows the measured threshold dispersions. The measured threshold dispersions for $V_{\rm TH1}$, $V_{\rm TH2}$, and $V_{\rm TH3}$ are 134 $\rm e^-$ rms, 144.5 $\rm e^-$ rms, and 164.3 $\rm e^-$ rms, respectively, without any calibration.

TABLE I
PERFORMANCE SUMMARY AND COMPARISON WITH PREVIOUS WORKS

	Gain (mV/ke$^-$)	Pixel # (Kpixel)	Pixel pitch (μm)	# of energy bins	Counter (bits)	Reset time (μs)	ENC (e^- rms)	Threshold dispersion* (e^- rms)	Pixel power (μW)
This work	**107**	**16**	**60**	**3**	**15**	**< 0.15**	**68 @ f_{In}= 1MHz**	**134 – 164**	**4.6**
Ref [5]	12.5	64	55	1	13	< 1	141 – 200	360 – 800	8
Ref [7]**	11.4	64	55	2	12	< 1.5 (HG) < 2.5 (LG)	60 (HG) 85 (LG)	1,000 (HG) 1,900 (LG)	9
Ref [8]	N/A	1	200	2	18	N/A	80 ± 20 (CdTe) 105 ± 20 (Si)	180	N/A
Ref [9]	10.9	N/A	109	3	12	a few	213	N/A	15
Ref [10]	N/A	1	500	1	8	8 – 10	N/A	N/A	770
Ref [11]	19.2	0.13	1,000	2	18	N/A	> 430	N/A	2,100
Ref [12]	N/A	0.26	100	1	10	1 – 10	N/A	N/A	20

* without calibration.
** [7] measured in single pixel mode.
HG: High gain mode / LG: Low gain mode

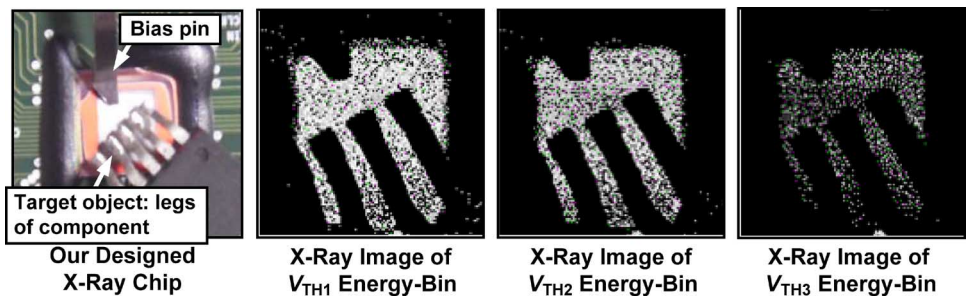

Fig. 24. X-ray images obtained from our designed X-ray chip.

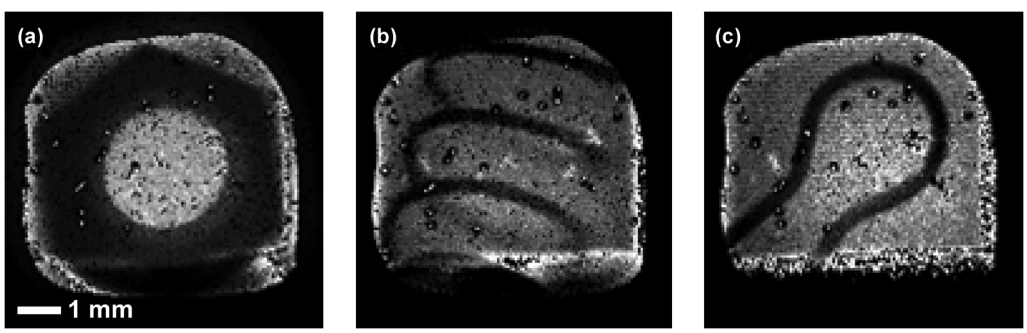

Fig. 25. Demonstrated single-energy X-ray images: (a) screw nut; (b) pen spring; (c) clip pin.

We performed real X-radiation experiments and successfully demonstrated real X-ray images. Fig. 24 shows multi-energy X-ray images obtained from our designed chip. In this experiment, the material used in the tube of the X-ray source was molybdenum (Mo) and the X-ray energy peaked at 49 kVp. The tube current was 50 mA. The X-ray target object was the metal legs of an IC package. As can be seen in the figure, the X-ray image of the metal legs was projected on our detector chip. Note that the X-ray photons are not able to transmit through metal. Fig. 25 also presents single-energy X-ray images captured by the proposed chip. Our X-ray image detector obtains high definition quality without image blurring owing to its high spatial resolution of 60 $\mu\mathrm{m/pixel}$. The reason for some defects in the obtained X-ray images is the low yield of the bump connection between the photoconductor and the detector pixel of the X-ray imager chip.

C. Performance Summary and Comparison With Prior Works

Table I compares the performances of the proposed X-ray photon counting image detector with those of state-of-the-art

detector chips [5], [7]–[12]. Thanks to the compact SAL ADC in our design, the pixel pitch of the proposed chip is only 60 μm despite the 3-level photon energy detection capability. Charge-to-voltage conversion gain of 107 $\mathrm{mV/ke^-}$ is achieved, which is more than five times higher than that of recently reported works. Due to the fast charge reset scheme, the time to return to baseline is under 150 ns. Also, each pixel consumes static power of only 4.6 μW, which is smaller than that of any previous works. The measured equivalent noise charge (ENC) is 68 $\mathrm{e^-\ rms}$ at the charge incoming frequency $f_{\mathrm{In}} = 1$ MHz. The measured maximum threshold dispersion is 164.3 $\mathrm{e^-\ rms}$ without any calibration. Since the proposed sampling-based operation allows dynamic offset cancellation, the measured threshold dispersion of our designed chip is relatively lower than that of previous works.

VI. Conclusion

A multi-energy and high spatial resolution X-ray photon counting image detector chip with low power consumption is presented in this paper. A robust sampling-based charge preamplifier with high charge-to-voltage conversion gain and fast reset speed is proposed. Additionally, sampling-based operation contributes to achieving high pixel-to-pixel uniform performance and low noise by the correlated double sampling. This paper also proposed an in-pixel SAL ADC (multi-energy discriminator) to minimize energy consumption and improve spatial resolution with 3-level discrimination of X-ray photon energies. The functionality of our work is also successfully demonstrated using real X-ray images. The proposed architecture and design approach is applicable to high quality medical X-ray image detectors with low radiation dosage to patients.

References

[1] R. Irsigler, J. Anderson, J. Alverbro, J. Borglind, C. Fröjdh, P. Helander, S. Manolopoulos, H. Martijn, V. O'Shea, and K. Smith, "X-ray imaging using a 320 × 240 hybrid GaAs pixel detector," *IEEE Trans. Nucl. Sci.*, vol. 46, no. 3, pp. 507–512, Jun. 1999.

[2] R. Steadman, F. M. Serrano, G. Vogtmeier, A. Kemna, E. Oezkan, W. Brockherde, and B. J. Hosticka, "A CMOS photodiode array with in-pixel data acquisition system for computed tomography," *IEEE J. Solid-State Circuits*, vol. 39, no. 7, pp. 1034–1043, July 2004.

[3] B. Mikulec, "Development of segmented semiconductor arrays for quantum imaging," *Nucl. Instrum. Methods Phys. Res., Sect. A, Accel. Spectrom. Detect. Assoc. Equip.*, vol. 510, pp. 1–23, Sep. 2003.

[4] I. Willekens, B. Dierickx, N. Buls, C. Breucq, A. Schiettecatte, J. D. Mey, and C. Bourgain, "Superiority of multi-energy color X-ray for breast specimen radiography," in *European Society for Radiography Congress*, Mar. 2011.

[5] X. Llopart, M. Campbell, R. Dinapoli, D. San Segundo, and E. Pernigotti, "Medipix2: A 64-k pixel readout chip with 55- μm square elements working in single photon counting mode," *IEEE Trans. Nucl. Sci.*, vol. 49, no. 5, pp. 2279–2283, Oct. 2002.

[6] R. Ballabriga, M. Campbell, E. H. M. Heijne, X. Llopart, and L. Tlustos, "The Medipix3 prototype, a pixel readout chip working in single photon counting mode with improved spectrometric performance," *IEEE Trans. Nucl. Sci.*, vol. 54, no. 5, pp. 1824–1829, Oct. 2007.

[7] R. Ballabriga, M. Campbell, E. Heijne, X. Llopart, L. Tlustos, and W. Wong, "Medipix3: A 64 k pixel detector readout chip working in single photon counting mode with improved spectrometric performance," *Nucl. Instrum. Methods Phys. Res., Sect. A, Accel. Spectrom. Detect. Assoc. Equip.*, vol. 633, pp. S15–S18, May 2011.

[8] M. Löcker, P. Fischer, S. Krimmel, H. Krüger, M. Lindner, K. Nakazawa, T. Takahashi, and N. Wermes, "Single photon counting x-ray imaging with Si and CdTe single chip pixel detectors and multichip pixel modules," *IEEE Trans. Nucl. Sci.*, vol. 51, no. 4, pp. 1717–1723, Aug. 2004.

[9] M. Perenzoni, D. Stoppa, M. Malfatti, and A. Simoni, "A multispectral analog photon-counting readout circuit for x-ray hybrid pixel detectors," *IEEE Trans. Instrum. Meas.*, vol. 57, no. 7, pp. 1438–1444, July 2008.

[10] K. Spartiotis, A. Leppänen, T. Pantsar, J. Pyyhtiä, P. Laukka, K. Muukkonen, O. Männistö, J. Kinnari, and T. Schulman, "A photon counting CdTe gamma- and X-ray camera," *Nucl. Instrum. Methods Phys. Res., Sect. A, Accel. Spectrom. Detect. Assoc. Equip.*, vol. 550, pp. 267–277, Sep. 2005.

[11] J. S. Iwanczyk, E. Nygård, O. Meirav, J. Arenson, W. C. Barber, N. E. Hartsough, N. Malakhov, and J. C. Wessel, "Photon counting energy dispersive detector arrays for x-ray imaging," *IEEE Trans. Nucl. Sci.*, vol. 56, no. 3, pp. 535–542, Jun. 2009.

[12] B. Dierickx, B. Dupont, A. Defernez, and N. Ahmed, "Indirect x-ray photon-counting image sensor with 27 T Pixel and 15 $\mathrm{e^-_{rms}}$ accurate threshod," in *IEEE Int. Solid-State Circuits Conf. Dig. Tech. Papers*, Feb. 2011, pp. 114–115.

[13] F. Krummenacher, "Pixel detectors with local intelligence: An IC designer point of view," *Nucl. Instrum. Methods Phys. Res., Sect. A, Accel. Spectrom. Detect. Assoc. Equip.*, vol. 305, pp. 527–532, Aug. 1991.

[14] E. Gatti and P. F. Manfredi, "Processing the signals from solid-state detectors in elementary-particle physics," *Rivista del Nuovo Cimento*, vol. 9, no. 1, pp. 1–146, 1986.

[15] V. Radeka, "Trapezoidal filtering of signals from large germanium detectors at high rates," *Nucl. Instrum. Methods*, vol. 99, pp. 525–539, Mar. 1972.

[16] M. Porro, C. Fiorini, and L. Strüder, "Theoretical comparison between two different filtering techniques suitable for the VLSI spectroscopic amplifier ROTOR," *Nucl. Instrum. Methods Phys. Res., Sect. A, Accel. Spectrom. Detect. Assoc. Equip.*, vol. 512, pp. 179–190, Oct. 2003.

[17] P. Grybos and R. Szczygiel, "Pole-zero cancellation circuit with pulse pile-up tracking system for low noise charge-sensitive amplifiers," *IEEE Trans. Nucl. Sci.*, vol. 55, no. 1, pp. 583–590, Feb. 2008.

[18] M.-J. Chen, Y.-B. Gu, T. Wu, P.-C. Hsu, and T.-H. Liu, "Weak inversion charge injection in analog switches," *IEEE J. Solid-State Circuits*, vol. 30, no. 5, pp. 604–606, May 1995.

[19] Y.-B. Gu and M.-J. Chen, "A new quantitative model for weak inversion charge injection in MOSFET analog switches," *IEEE T. Electron Devices*, vol. 43, no. 2, pp. 295–298, Feb. 1996.

[20] H.-S. Kim, S.-W. Han, J.-H. Yang, S. Kim, Y. Kim, S. Kim, D.-K. Yoon, J.-S. Lee, J.-C. Park, Y. Sung, S.-D. Lee, S.-T. Ryu, and G.-H. Cho, "A sampling-based 128 × 128 direct photon-counting x-ray image sensor with 3 energy bins and spatial resolution of 60 $\mu\mathrm{m/pixel}$," in *IEEE Int. Solid-State Circuits Conf. Dig. Tech. Papers*, Feb. 2012, pp. 110–111.

[21] S. I. Kim, S. W. Kim, J. C. Park, Y. Kim, S. W. Han, H. K. Kim, C. J. Kim, U.-I. Chung, I.-K. Yoo, and K. Kim, "Highly sensitive and reliable X-ray detector with $\mathrm{HgI_2}$ photoconductor and oxide drive TFT," in *IEEE Int. Electron Devices Meeting Dig. Tech. Papers*, Dec. 2011, pp. 14.2.1–14.2.4.

[22] F. Anghinolfi, P. Aspell, K. Bass, W. Beusch, L. Bosisio, and C. Boutonnet *et al.*, "A 1006 element hybrid silicon pixel detector with strobed binary output," *IEEE Trans. Nucl. Sci.*, vol. 39, no. 4, pp. 654–661, Aug. 1992.

Hyun-Sik Kim (S'11) received the B.S. degree with highest honors from Hanyang University, Seoul, Korea, in 2009, and the M.S. degree from KAIST, Daejeon, Korea, in 2011, both in electrical engineering. Since 2011, he has been working toward Ph.D. degree in electrical engineering at KAIST, Daejeon, Korea.

His research interests are in the field of CMOS analog integrated circuit design, and his current research areas are focused on mixed-signal circuits, flat panel display drivers, and X-ray image sensors.

Mr. Kim won a Gold Medal in the 18th Human-Tech Thesis Prize hosted by Samsung Electronics in 2012.

Sang-Wook Han received the B.S., M.S., and Ph.D. degrees in electrical engineering from Korea Advanced Institute of Science and Technology (KAIST), Daejeon, Korea, in 1999, 2001, and 2006, respectively.

From 2006 to 2009, he worked for the Pixelplus Corporation, Gyeonggi-do, Korea, where he is working on the development of various CMOS imagers. From 2009 to 2012, he was a Research Staff at Samsung Advanced Institute of Technology, Gyeonggi-do, Korea, where he engaged in researching high sensitivity CMOS imagers and photon counting X-ray detector. In 2012, he joined Korea Institute of Science and Technology (KIST), Seoul, Korea. His research interests are in single photon detector, quantum cryptography, CMOS imagers, fingerprint sensors, and VLSI system design.

Jun-Hyeok Yang received the B.S. degree from Kyung-Pook National University, Daegu, Korea, in 2007 and the M.S. degree in electrical engineering from KAIST (Korea Advanced Institute of Science and Technology), Daejeon, Korea, in 2009. He is currently pursuing the Ph.D. degree in electrical engineering at KAIST.

His research interests are in the field of analog integrated circuit design, and his current research areas are in the TSP (Touch Screen Panel) readout ICs, AMOLED display drivers, and X-ray photon-counting detector ICs.

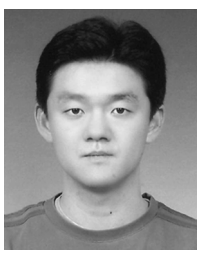

Sunil Kim received the M.Sc. and Ph.D. degrees in Material Science and Engineering at the Korea Advanced institute of Science and Technology in Korea in 2001 and 2006. He joined SAIT (Samsung Advanced institute of Technology) in Korea, where his research interests are oxide thin film transistor and photoconductor for X-ray detector.

Young Kim received the B.S. and M.S. degrees in electrical engineering at Kwangwoon University, Seoul, Korea, in 2003 and 2005, respectively.

From 2005 to 2010, he worked at the System IC Laboratory of CTO affiliation of LG Electronics, Seoul, Korea, as a senior research engineer for Mobile AMOLED and LCD Driver IC.

He is currently a research staff member at Samsung Advanced Institute of Technology, Yongin, Korea. His main research interests are currently in medical image sensor.

Sangwook Kim, photograph and biography not available at the time of publication.

Dae-Kun Yoon received the B.S. and M.S. in electrical engineering from Korea Advanced Institute of Science and Technology (KAIST), Daejeon, Korea, in 2003 and 2005, respectively.

From 2005 to 2011, he worked at the Advanced Circuit Design Group, Hynix semiconductor, Korea, where his research interests are analog, mixed-signal for GDDR5 SDRAM, DRAM interface chip applications. In 2011, he joined a Research Staff at the Semiconductor Lab, Samsung Advanced Institute of Technology, Gyeonggi-do, Korea, where his research interests are X-ray photon counting detector design.

Jun-Su Lee was born in South Korea in 1970. He received the M.Sc. degree in metallurgical engineering from Yonsei University, Seoul, Korea, in 1999. From 2000 to 2001, he worked as an Intern Researcher, within the metal processing research center of the Materials Science and Technology Division, Korea Institute of Science and Technology (KIST), Seoul, Korea. He received the Ph.D. degree in electrical and electronic engineering at Imperial College London, U.K. in 2006. He worked as a senior researcher at Amkor Technology Korea, from 2006 to 2010. He is currently working as a research staff at Samsung Advanced Institute of Technology (SAIT).

Jae-Chul Park, photograph and biography not available at the time of publication.

Younghun Sung, photograph and biography not available at the time of publication.

Seong-Deok Lee received the B.S. and M.S. degrees in electronics engineering at Kwang-Woon University, Seoul, Korea, in 1987 and 1989, respectively.

He joined Samsung Advanced Institute of Technology (SAIT), Suwon, Korea, where his research interests are color vision, image processing and image capturing for consumer electronics and Medical imaging devices. Currently, he is director of the Medical Imaging Group in SAIT.

Seung-Tak Ryu (M'06) received the B.S. degree in electrical engineering from Kyungpook National University, Korea, in 1997, and the M.S. and Ph.D. degrees from Korea Advanced Institute of Science and Technology (KAIST) in 1999 and 2004, respectively. From 2001 to 2002, he was with University of California at San Diego as a visiting researcher sponsored through the Brain Korea 21 (BK21) program. In 2004, he joined Samsung Electronics, Kiheung, Korea, where he was involved in mixed-signal IP design. From 2007 to 2009, he was with the Information and Communications University (ICU), Daejeon, Korea, as an Assistant Professor. He has been with the Department of Electrical Engineering, KAIST, Daejeon, Korea, since 2009, where he is currently an Associate Professor. His research interests include analog and mixed-signal IC design with an emphasis on data converters.

Gyu-Hyeong Cho (S'76–M'80–SM'11) received the B.S. degree from Hanyang University, Korea, and the M.S. and Ph.D. degrees from the Korea Advanced Institute of Science and Technology (KAIST) in 1975, 1977, and 1981, respectively, all in electrical engineering.

During 1982–1983, he was with the Westinghouse R&D Center in Pittsburgh, PA. In 1984, he joined the Department of Electrical Engineering at KAIST where he has been a full Professor since 1991. His early research was in the area of power electronics until the late 1990s and worked on soft switching converters and high power converters. Later, he shifted to analog integrated circuit design, and now he is interested in several areas including power management ICs, Class-D amplifiers, touch sensors and drivers for AMOLED and LCD flat panel displays and biosensors. He has authored one book on advanced electronic circuits and authored or coauthored over 200 technical papers and 80 patents.

Dr. Cho received the Outstanding Teaching Award from KAIST. He was a corecipient of the Silkroad Award and guest editor at the ISSCC in 2007 and 2010, respectively. He served as a member of the ISSCC international technical program committee, and is now an associate editor of IEEE JOURNAL OF SOLID-STATE CIRCUITS.